Physics of Fluids

RESEARCH ARTICLE | MARCH 19 2026

Experimental investigation of cavitation dynamics at mesoscale and microscale in swirled and non-swirled venturi tubes

M. Shahsavari ; D. Eakins ; P. Vagovič ; H. Soyama ; J. C. P. Koliyadu ; T. Sato ; R. Graceffa ; A. Mazzolari ; Š. Birnšteinová ; D. Moško ; P. Szeles ; J. Uličný ; W. Yashiro ; A. Meents

Check for updates

Physics of Fluids 38, 033335 (2026)
https://doi.org/10.1063/5.0310693

View Online
Export Citation

Articles You May Be Interested In

Full three-dimensional computational fluid dynamics simulation and optimization of a swirling jet-induced cavitation reactor

Physics of Fluids (August 2023)

Experimental Study on Performance of Turbine Flowmeter and Venturi Meter in Oil-Water Two-Phase Flow Measurement

AIP Conf. Proc. (June 2007)

Improved semi-theoretical correlation to predict the Sauter mean diameter of swirl cups

Physics of Fluids (May 2024)

22 April 2026 09:41:02

AIP Advances
Why Publish With Us?
21DAYS average time to 1st decision
OVER 4 MILLION views in the last year
INCLUSIVE scope
Learn More
AIP Publishing

AIP Publishing

Physics of Fluids ARTICLE pubs.aip.org/aip/pof

Experimental investigation of cavitation dynamics at mesoscale and microscale in swirled and non-swirled venturi tubes

Cite as: Phys. Fluids **38**, 033335 (2026); doi: 10.1063/5.0310693
Submitted: 4 November 2025 · Accepted: 23 February 2026 ·
Published Online: 19 March 2026

View Online Export Citation CrossMark

M. Shahsavari,[1] D. Eakins,[1,a)] P. Vagovič,[2,3] H. Soyama,[4] J. C. P. Koliyadu,[2] T. Sato,[2] R. Graceffa,[2] A. Mazzolari,[5] Š. Birnšteinová,[2] D. Moško,[6] P. Szeles,[6] J. Uličný,[6] W. Yashiro,[7] and A. Meents[3]

AFFILIATIONS

[1]Department of Engineering Science, University of Oxford, Parks Road, Oxford OX1 3PJ, United Kingdom
[2]European XFEL GmbH, Holzkoppel 4, 22869 Schenefeld, Germany
[3]Center for Free-Electron Laser Science CFEL, Deutsches Elektronen-Synchrotron DESY, Notkestr. 85, Hamburg 22607, Germany
[4]Department of Finemechanics, Tohoku University, Sendai 980-8579, Japan
[5]INFN Sezione di Ferrara, Via Saragat 1, Ferrara 44122, Italy
[6]Faculty of Science, Department of Biophysics, P. J. Šafárik University, Jesenná 5, 04154 Košice, Slovakia
[7]Department of Applied Physics, School of Engineering, The University of Tokyo, 7-3-1 Hongo, Bunkyo-ku, Tokyo 113-8656, Japan

[a)]**Author to whom correspondence should be addressed:** daniel.eakins@eng.ox.ac.uk

ABSTRACT

Hydrodynamic cavitation has been widely used in various applications, namely, peening, surface cleaning, and wastewater treatment. Recent studies have demonstrated that introducing swirl in hydrodynamic cavitation can substantially enhance process efficiency. However, a knowledge gap remains regarding the comparative characteristics of hydrodynamic cavitation in swirled and non-swirled flows at the mesoscale and microscale. In this study, we utilize shadowgraph and high-speed phase-contrast x-ray imaging techniques alongside spectral proper orthogonal decomposition to resolve such characteristics in venturi tubes. The analyses show that imposing swirl reduces the hydraulic power delivered by the pump to initiate cavitation by 71.9%. It also makes the cavitating length of the flow less dependent on the operating condition. Investigations indicate that the non-swirled venturi tube is dominated by sheet cavitation followed by cloud cavitation. Introducing swirl shifts the cavitation toward the cloud regime established at the center of the tube while changing the coherent motions of the cavitating flow. In non-swirled flow, coherent motions are dominated by disk-like structures, while in the swirled flow, they include helical and double-helical coherent structures. Both mesoscale and microscale analyses reveal that swirl shifts the cavitation dynamics toward low-frequency coherent motions. Microscale results suggest that microbubbles from cavitation cloud collapse could trigger cavitation when they are involved in high-velocity motions.

© 2026 Author(s). All article content, except where otherwise noted, is licensed under a Creative Commons Attribution (CC BY) license (https://creativecommons.org/licenses/by/4.0/). https://doi.org/10.1063/5.0310693

I. INTRODUCTION

Hydrodynamic cavitation is the formation of vapor cavities in liquids when the local liquid pressure drops below the vapor pressure due to flow acceleration.[1] This phenomenon commonly occurs in applications such as fuel injectors and orifice plate throttling devices.[2] In these applications, cavitation can promote atomization and mixing processes, while it may result in erosion and limit the maximum flow rate.[3–7] Hydrodynamic cavitation is also utilized in various other applications, namely, cavitation peening,[8–11] surface cleaning,[12–14] and water treatment,[15,16] to leverage the energy harnessed by cavitation collapse. In these applications, cavitation features, including coherent and unsteady motions, govern the effectiveness of the processes. Hydrodynamic cavitation is commonly studied in venturi tubes, enabling well-controlled and repeatable experiments.[17–19]

Several valuable studies have been devoted in the past to characterizing mesoscale features of hydrodynamic cavitation in venturi tubes.[20–22] The investigations have shown that cavitation in venturi tubes can be classified into two dominant modes, termed "sheet" and

22 April 2026 09:41:02

© Author(s) 2026

"cloud."[23–25] Sheet cavitation is formed near the throat of a venturi tube when the flow passes low-pressure regions near the walls.[26–28] One of the mechanisms to sustain this regime is by trapping microbubbles where the boundary layer is thickened.[29] Flow disturbances can initiate the shedding of vapor bubbles from the thin glossy sheet of cavities and generate bubble clouds that move freely in the flow.[5] Contamination, e.g., solid particles, can also contribute to sustaining these regimes by acting as cavitation nuclei.[30] According to the previous studies, two mechanisms can cause periodic cavitation shedding in venturi tubes: re-entrant jet and bubbly shock (condensation shock) mechanisms.[31,32] The re-entrant jet mechanism consists of a liquid flow motion developed due to an adverse pressure gradient.[33,34] This jet-like motion penetrates between a sheet cavitation and walls from the cavity closure with a velocity of 20%–30% of the free-stream velocity.[35] Previous investigations have shown that when the re-entrant jet is thick enough, it can partially or even completely pinch off the sheet cavitation, thus initiating cavitation shedding.[36,37] This mechanism is also one of the mechanisms controlling cavitation shedding in submerged cavitating jets impinging on a specimen, where the jet–wall distance significantly alters the shedding features and cavitation cloud formation on the specimen.[38] Unlike the re-entrant jet mechanism, which is the dominant driver for cavitation shedding at low pressure ratios, i.e., low flow acceleration, the condensation shock mechanism governs the shedding at high flow acceleration values.[39,40] The bubbly shock mechanism occurs when a cavitation cloud collapses, producing a spherical shock wave.[32,39] This shock wave propagating toward the throat detaches cavities from their inception point, triggering cavitation shedding.[5,41] Both re-entrant jet and bubbly shock mechanisms involve coherent motions of vapor. However, coherent motions associated with the bubbly shock are noticeably larger than those originating from the re-entrant jet.[42]

Hydrodynamic cavitation exhibits various additional types of coherent motions,[26] which have significant effects on cavitation properties, including shedding dynamics, instantaneous overpressures, and chaotic entrainment.[5,33,35] In turbulent cavitating jets, vortex ring-shaped structures have been reported near the jets,[43–45] which are formed by the axisymmetric instability mode. The size and shedding frequency of these structures can be controlled by incorporating Helmholtz resonators, which can drive self-excited instabilities followed by coherent cavitation.[46] Further downstream of the jet, coherent motions turn into helical-like structures triggered by non-axisymmetric instability modes.[47,48] This phenomenon has also been observed in both cylindrical cyclones used for oil–water separation[49] and regulating valves.[50] However, cavitation is not necessarily associated with local low pressure in the core of coherent turbulent eddies.[26] Hairpin-shaped coherent motions are reported in cavity closures due to shear layer roll-up.[51] The height of these structures can be up to three times larger than that of the stable cavity from which they evolve.[27] These structures dominate the flow dynamics downstream of the stable cavity and involve substantial vorticity.[27] The collapse of these structures has been found to correlate with the luminescence intensity of cavitation in venturi tubes.[52] In the jet in cross-flow configuration, the shedding frequency of these structures decreases with the reduction of the cavitation number.[51] Another coherent structure in cavitation is wave-like cavities formed in shear layers due to Kelvin–Helmholtz instabilities,[23,51] which can evolve into large-scale structures due to vortex pairing.[53] In applications with abrupt pressure and area changes, such as marine turbomachinery, tip leakage and helical structures have been observed, leading to significant erosion, acoustic noise, and structural vibration.[54–57] Helical-like and vortex rope structures have also been reported in applications involving swirling motions, e.g., vortex diodes in water treatment,[58,59] and self-excited oscillating cavitation nozzles.[60]

Visualizing coherent structures in cavitation is not always straightforward, as they can include chaotic, multimodal, and intermittent features.[61–63] The most well-known method for extracting the spatial distribution of such features is energy-ranked proper orthogonal decomposition (POD).[64–68] In this method, data are decomposed into orthogonal modes, which are then ranked based on their energy content.[69] A more advanced class of this method is spectral proper orthogonal decomposition (SPOD), which enables characterizing both spatial and temporal features of coherent motions.[70] Considering studies on cavitation in venturi tubes, Xu *et al.* used POD to experimentally evaluate the mesoscale characteristics of the most energetic modes of sheet and cloud cavitation regimes, as well as cavitation shedding by re-entrant jet and bubbly shock in a venturi tube.[25,71] Using a similar analysis, Danlos *et al.* explored the effects of grooved surfaces in venturi tubes on coherent motions.[72] They showed that grooves significantly suppress cloud cavitation, potentially reducing cavitation erosion.[72] Gouin *et al.* applied SPOD to numerical results obtained by using a Reynolds-averaged Navier–Stokes solver to study coherent motions in the sheet cavitation regime. They concluded that these motions exhibit asymmetric behavior in the streamwise and spanwise directions.[28]

Although few studies have addressed microscale features of hydrodynamic cavitation in venturi tubes, substantial efforts have been made to improve the understanding of microscale features of cavitation in highly controllable cavitation devices, namely, laser or electrical discharge induced cavitation.[73–76] The corresponding findings have implications for hydrodynamic cavitation, which comprises a cascade of multidimensional bubbles. These studies have shown that cavitation may involve high-velocity micro-jets, depending on the proximity of a cavitation bubble to a wall or an adjacent air or cavitation bubble.[74,77,78] As the bubble–wall distance decreases, the micro-jet deforms the bubble into a more asymmetric shape near the moment of collapse.[79,80] The micro-jet direction in a single bubble configuration is toward the nearest wall,[81,82] while in bubble clusters, the bubble–bubble and bubble–wall distances can alter the micro-jet direction and velocity.[74,83] Cavitation may involve complex jetting modes, when a bubble is placed near multiple rigid and deformable surfaces, including fracture-redirected jet, bisector jet, divergent jet, and split jet.[84] Cavitation bubble collapse also results in short-lived intense pressure waves.[85] The amplitude of such pressure waves increases as the bubble–wall distance decreases.[78,86] In bubble cluster configurations, the intensity of shock waves responds non-monotonically to the relative distance between the bubbles.[87,88]

Previous studies have shown that introducing swirl in venturi tubes and orifices moves cavitating regions toward the center of the tube, reducing the pressure loss and the risk of inner wall erosion.[89–91] Additionally, in particular applications of hydrodynamic cavitation, such as wastewater treatment, it has been reported that swirl enhances the process efficiency, e.g., improving particle separation, slug disintegration, solvent degradation, and disinfection.[90,92–95] However, there is still no explicit explanation for such performance enhancements, nor

22 April 2026 09:41:02

© Author(s) 2026

detailed comparisons between the distinct features of swirled and non-swirled cavitating flows.

Encouraged by the promising performance of cavitation-based wastewater treatment methods incorporating swirling flows and aiming to address the knowledge gap regarding the key features of swirled and non-swirled hydrodynamic cavitation, this study was conceived to evaluate, for the first time, the mesoscale and microscale characteristics of hydrodynamic cavitation in venturi tubes, both with and without swirl. We use shadowgraph and high-speed phase-contrast x-ray imaging techniques alongside SPOD analyses to characterize key features of swirled and non-swirled cavitating flows. This study offers new insights into the effects of swirl on hydrodynamic cavitation, with potential implications for applications that leverage hydrodynamic cavitation, such as cavitation peening, surface treatment, and wastewater treatment, to configure hydrodynamic cavitation and enhance process efficiency. This paper is structured as follows: Sec. II outlines the methodology. The results obtained are presented in Sec. III, followed by the conclusions in Sec. IV.

II. METHODOLOGY

A. Experimental apparatus

The experiments were conducted using a cavitation apparatus shown schematically in Fig. 1. The apparatus consisted of a closed hydraulic loop, equipped with a sample environment, as well as mesoscale and microscale imaging setups. In the hydraulic loop, a diaphragm pump was used to circulate water in the loop. Two sets of pressure indicators and transmitters were used on the sides of the sample environment to monitor and measure the flow pressure, respectively. The accuracy of the pressure transmitters was less than ±0.5% of the four-bar full-scale range. Moreover, a valve was used downstream of the sample environment to adjust the back pressure. The water volume flow rate was measured using an inline turbine flow transmitter with accuracy, repeatability, and maximum pressure drop of ±2%, ±1%, and 0.1 bar, respectively. The measured flow rate, alongside the water density obtained from the NIST database, was used to estimate the flow velocity at the throat, U_t. The water temperature was measured using a type T thermocouple with an accuracy of ±0.1 °C. A NI DAQ device integrated with LabVIEW software was used to acquire the pressure and flow rate measurements simultaneously and control the valve.

Figure 2 shows the sample environments utilized in this study to evaluate the effects of swirl on mesoscale and microscale characteristics of hydrodynamic cavitation. Sample VTns is a conventional venturi tube with a throat diameter, D, of 1.5 mm and a divergence angle of 14° to avoid flow separation.[96] In hydrodynamic cavitation, swirl can be introduced in venturi tubes by placing guide vanes in the flow path[58] or equipping the venturi tubes with a vortex chamber and tangential flow inlets.[89,97] The latter has been used more frequently in cavitation devices, e.g., in water treatment, thanks to its low pressure drop. We used a similar method to generate swirling motions in venturi tubes in the second sample, i.e., VTs, as shown in Fig. 2(b). This venturi tube involves a chamber with a cylindro-conical shaped bluff body at the center and a tangential flow inlet [Fig. 2(c)]. Samples VTns and VTs have the same throat diameter and divergence angle, which were printed with a Formlabs (Form 3L) 3D printer using clear resin with a resolution of 50 μm and a wall thickness of 1 mm. The samples were connected via long tubes to the pressure transmitters and flow meter to ensure that the flow field is fully developed for precision measurements of pressure and volume flow rate.

B. Visualization

As schematically shown in Fig. 1, two sets of imaging techniques were used to visualize the mesoscale and microscale characteristics of hydrodynamic cavitation. The mesoscale visualization technique is based on shadowgraph imaging and consists of a 120 W LED light source and a kilohertz-rate high-speed Phantom camera (V7.3) equipped with a Nikon AF Micro lens with a focal length of 60 and 32 mm macro extension tubes. The samples were placed between the uniform light source and the high-speed camera. Using this configuration, the cavitation scatters the light, resulting in darker regions in the images. The exposure time, the sampling frequency, and recording time of the camera were set at 1 μs, 20 kHz, and 1 s, respectively. The field of view covered by this technique was $15.36 \times 7.68\,\text{mm}^2$, and the pixel size was 30 μm. The microscale visualization was carried out at the Single Particles, Clusters and Biomolecules and Serial Femtosecond Crystallography (SPB/SFX) instrument of the European XFEL.[98–100] This scientific instrument uses an indirect x-ray microscope with a fast camera to capture images at a megahertz repetition rate. The SPB/SFX instrument provides x-ray pulses in a burst mode with a burst length of 600 μs and a repetition rate of 10 Hz. Each burst contains x-ray

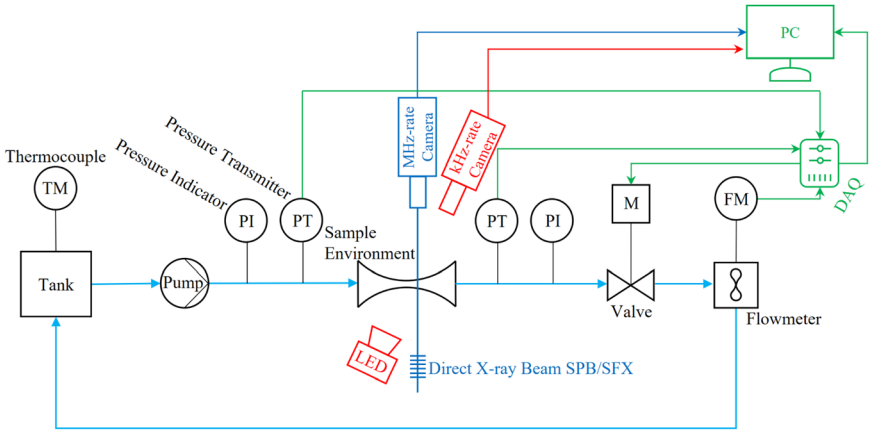

FIG. 1. Schematic of the experimental setup. In this setup, temperature was monitored using a thermocouple (TM), while pressure was measured using pressure transmitters (PTs) and was monitored using pressure indicators (PIs). The flow rate was measured using a flowmeter (FM), and the valve position was adjusted by a motor (M). High-speed imaging was performed using a kilohertz-rate camera and a megahertz-rate camera, which were synchronized with an LED light source and the x-ray pulses at the European XFEL, respectively.

22 April 2026 09:41:02

© Author(s) 2026

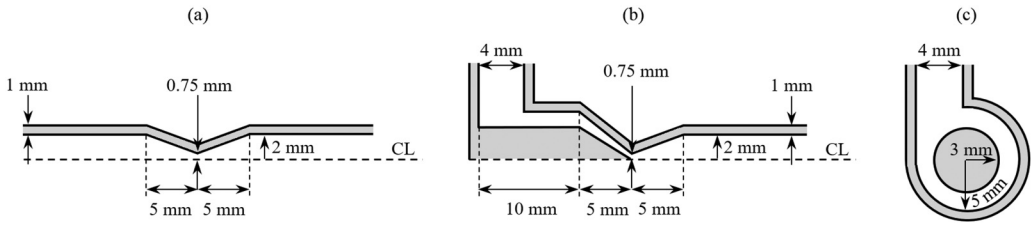

FIG. 2. (a) Side view cross section of the venturi tube without swirl (VTns), (b) side view cross section of the venturi tube with swirl (VTs), and (c) back view of VTs showing the tangential flow inlet. The dashed line indicates the centerline (CL). All dimensions are given in millimeters.

pulses at a megahertz repetition rate.[98,99] The megahertz-rate camera was synchronized with the burst of x rays to record 128 frames per burst with a frame rate frequency of 1.13 MHz. We recorded images in 18 successive trains in each experiment using two sets of spatiotemporal resolutions: 10 and 5× magnifications to resolve different microscale characteristics of the investigated cases. In 10× magnification, the field of view was $1.28 \times 0.8\,\text{mm}^2$, and the pixel size was $3.2\,\mu\text{m}$. Using 5× magnification, the spatial resolution was $6.4\,\mu\text{m}$, while the field of view was $2.56 \times 1.6\,\text{mm}^2$. In both cases, the beam size was 1.5 mm within the sample environment with a photon energy of 10 keV.

C. Experimental procedure and conditions

In this study, the cavitation number was defined as[101]

$$\sigma = \frac{p_1 - p_{vap}}{p_1 - p_2}, \tag{1}$$

where p_1 is the flow pressure upstream of the venturi tubes, p_{vap} is the vapor pressure, and p_2 is the flow pressure downstream of the venturi tubes. Here, p_1 and p_2 were measured using the pressure transmitters. The instantaneous and mean values of p_1 and p_2 were continuously monitored throughout the experiments and used to establish the operating condition at the start of each experiment based on predefined test conditions. Additionally, p_{vap} was obtained from the NIST database.

Experiments were performed at p_1 values ranging from 0.06 to 0.40 MPa in increments of 0.02 MPa, while maintaining the water temperature at 30 °C. The corresponding range of cavitation numbers investigated was $1.24 \leq \sigma \leq 2.62$. The standard uncertainty of the cavitation number, evaluated using first-order uncertainty propagation as detailed in the Appendix, is less than 0.004. Each experiment was started by adjusting the pump speed to match a pre-calculated cavitation number. Then, the system was allowed to run for a few minutes to stabilize the flow pressure.

Our investigations showed that the inception cavitation number in the VTns venturi tube is 1.70, while that in the VTs is 2.62. The corresponding inception volume flow rates for these cases are 2.18 and $1.43\,\text{l min}^{-1}$, respectively. Additionally, the pressure rise by the pump measured by the pressure transmitters to initiate cavitation is 0.14 MPa in the VTns venturi tube, while it is 0.06 MPa in the VTs venturi tube. Calculating the hydraulic power of the pump using Eq. (2) shows that incorporating swirl reduces the hydraulic power delivered by the pump, P_h, to achieve cavitation inception by 71.9%, a noticeable energy savings. Using first-order uncertainty propagation detailed in the Appendix, the relative standard uncertainty of hydraulic power is less than 3.2%,

$$P_h = \dot{Q}\Delta p, \tag{2}$$

where $\dot{Q}$ is the water volume flow rate and Δp is the pressure rise across the pump. Our preliminary studies for a wide range of cavitation numbers, i.e., $1.24 \leq \sigma \leq 2.62$, indicated that cavitation occurs consistently over time for cavitation numbers between 1.27 and 1.49, while the cavitating length of the tube lies within the field of view of the mesoscale visualization technique. Therefore, this range of cavitation numbers was considered in Sec. III to comparatively study cavitation features in the non-swirled and swirled venturi tubes.

D. Spectral proper orthogonal decomposition

We employed the spectral proper orthogonal decomposition method developed by Sieber *et al.*[70] to evaluate the spatiotemporal characteristics of coherent motions in hydrodynamic cavitation. This method is an extension of the classical energy-ranked POD, combining the capabilities of POD and the frequency-ranked discrete Fourier transform method, i.e., accurate estimations of spatial and temporal characteristics of coherent structures, respectively.[70] Using this method, first, the grayscale level of the flat-fielded images, I, was decomposed into averaged and fluctuating, I', parts as

$$I(i,j,n) = \left[\frac{1}{N}\sum_{k=1}^{N} I(i,j,k)\right] + I'(i,j,n), \tag{3}$$

where n is the frame number in a set of successor grayscale images, N is the total number of images, and i and j are the horizontal and vertical indices of pixels, respectively. Then, the fluctuating part was decomposed into a sum of spatial modes as follows:

$$I'(i,j,n) = \sum_{k=1}^{N} a_k(n)\Phi_k(i,j), \tag{4}$$

where Φ_k are the orthogonal basis functions (spatial modes) that best resolve modes and a_k are the corresponding temporal coefficients of modes, showing how strongly modes are present. To determine the spatial modes and their temporal coefficients, first, we calculated the cross correlations between the fluctuating parts of images, defined as the inner product of I' of the corresponding frames. Then, the temporal correlation matrix was constructed as follows:

$$C_{nn'} = \frac{1}{N}\langle I'(i,j,n), I'(i,j,n')\rangle, \tag{5}$$

22 April 2026 09:41:02

© Author(s) 2026

where $\langle .,. \rangle$ is the inner product integrated over all pixels. Here, a symmetric finite response filter was applied to the correlation matrix using the following equation to calculate the filtered temporal correlation matrix, $\tilde{C}_{nn'}$:

$$\tilde{C}_{nn'} = \sum_{f=-N_f}^{N_f} g_f C_{n+f,n'+f}, \tag{6}$$

where N_f is the filter size and g_f is a Gaussian filter coefficient vector. The eigenvalues, λ_k, and eigenvectors, v_k, of the filtered temporal correlation matrix were obtained by solving

$$\tilde{C}_{nn'} v_k = \lambda_k v_k, \tag{7}$$

where eigenvalues represent the mode energies, and eigenvectors are

$$v_k = [a_k(n=1), \ldots, a_k(n=N)]^T. \tag{8}$$

Finally, the spatial modes were obtained by projecting the data onto the temporal coefficients. This can be achieved by multiplying Eq. (4) by $a_m(n)$ and summing the equation over the images as

$$\sum_{n=1}^{N} I'(i,j,n) \cdot a_m(n) = \sum_{k=1}^{N} \Phi_k(i,j) \sum_{n=1}^{N} a_k(n) \cdot a_m(n). \tag{9}$$

Here, the temporal coefficients are orthogonal, and their inner product is

$$\sum_{n=1}^{N} a_k(n) \cdot a_m(n) = \lambda_k N \delta_{km}, \tag{10}$$

where δ_{km} is the Kronecker delta function. Incorporating Eq. (10) into Eq. (9) for $m = k$ results in the following expression for each spatial mode:

$$\Phi_k(i,j) = \frac{1}{\lambda_k N} \sum_{n=1}^{N} I'(i,j,n) \cdot v_k(n). \tag{11}$$

In this study, the frequency of each mode was evaluated by taking the fast Fourier transformation of the temporal coefficients.

III. RESULTS AND DISCUSSION

A. Mesoscale characteristics

Figure 3 shows the time sequences of the spatial distribution of cavitation in VTns and VTs venturi tubes for $\sigma = 1.4$ and 1.3, where t_0 denotes the time of the first frame presented in each image series. Here, spatial coordinates were normalized by the throat diameter, while positioning the origin of the coordinate system at the center of the throat. Moreover, flat-fielded images were binarized using the IsoData global thresholding algorithm[102] to improve the visibility of the cavitation structures. To assess the sensitivity of the results on the binarization method, we also used the Otsu binarization method.[103] Comparing the results using these methods showed that the proportion of pixels labeled differently by the two methods is 2.3%.

Comparing VTns and VTs venturi tubes at $\sigma = 1.4$ [Figs. 3(a) and 3(b)] shows that cavitation in VTs is more stable than that in VTns. Decreasing the cavitation number results in fully developed cavitation in both cases, as shown in Figs. 3(c) and 3(d), while enlarging the size of the cavitating regions. According to Figs. 3(a) and 3(c), as the non-swirled flow moves in the axial direction (x axis), the cavitating flow evolves into disk-like structures, which are flattened and approximately symmetric in the x direction. This cavitation shedding type is generally caused by re-entrant jet formation and adverse pressure gradients in the flow, which disrupt the cavity interface and release a pocket of cavities.[5,35,36] The results show that disk-like structures enlarge in size as the cavitation number decreases, presumably due to stronger cavitation at lower cavitation numbers. Figure 3 also reveals that introducing the swirl significantly changes the overall features of cavitation. The distinct features of cavitation in VTs when compared to those in VTns are the helical-like and double helical-like structures, which exhibit a twisted, three-dimensional shape and are asymmetric in both x and y directions. Some of these structures are shown in Figs. 3(b-I) and 3(b-IV) and 3(d-III) and 3(d-IV). These structures are believed to be generated due to the non-axisymmetric instability modes introduced by the combination of the Kelvin–Helmholtz and centrifugal instabilities.[104–106] The Kelvin–Helmholtz instability triggers the formation of a ring-like vortex structure, and the centrifugal instability organizes the structures in a helical-like pattern. The double helical-like structures are fundamentally due to either the intertwining of two helical-like structures or the vortex pairing process, which is further discussed in Sec. III B. Cavitation in the VTns venturi tube rarely involves helical-like structures, like the one in Fig. 3(c-II), which are believed to be due to the activation of the non-axisymmetric instability modes as the non-swirled venturi flow evolves in the axial direction.

Figure 3 also shows that the length of the cavitation zone in the axial direction varies significantly with the cavitation number. To quantify such changes, first, the averaged flat-fielded grayscale images were obtained by using 20 000 images. Then, as schematically shown in the inset of Fig. 4, the cavitating length of the venturi tubes in the averaged images, $\langle L_c \rangle$, was obtained by measuring the distance between the tip of the cavitating region and the throat. The results presented in Fig. 4 show that the cavitating length increases with decreasing cavitation number. Interestingly, $\langle L_c \rangle$ is less sensitive to σ in the swirled case compared with that in the non-swirled venturi tube. Comparing $\langle L_c \rangle$ in VTns and VTs tubes also shows that the cavitating length is noticeably higher in VTns at low cavitation numbers, whereas VTs exhibits a longer $\langle L_c \rangle$ at high cavitation numbers. The latter is attributed to the more stable cavitation in VTs, which can be found by comparing Figs. 3(a) and 3(b), resulting in a longer cavitating length in this venturi tube than that in VTns. Figure 3 also shows that cavitation in VTns involves more cavitation shedding and disjoined structures than VTs. These structures, e.g., disk-like structures, persist for a specific distance from the throat before collapsing. The results show that decreasing the cavitation number significantly enlarges the disk-like structures and the main body of the cavitating region attached to the throat. This, in turn, contributes to increasing $\langle L_c \rangle$ in VTns at low cavitation numbers.

To quantify the characteristics of the coherent structures illustrated in Fig. 3, Figs. 5(a) and 5(b) present the averaged values of the cavitation shedding length, $\langle L_s \rangle$, and pitch, $\langle L_p \rangle$, as a function of the cavitation number in VTns and VTs venturi tubes, respectively. Here, L_s was defined as the averaged axial distance between the center of adjacent disk-like structures and that between the center of the first observable structure and the edge of the attached cavity near the throat. Additionally, L_p is the axial distance between two points on

22 April 2026 09:41:02

© Author(s) 2026

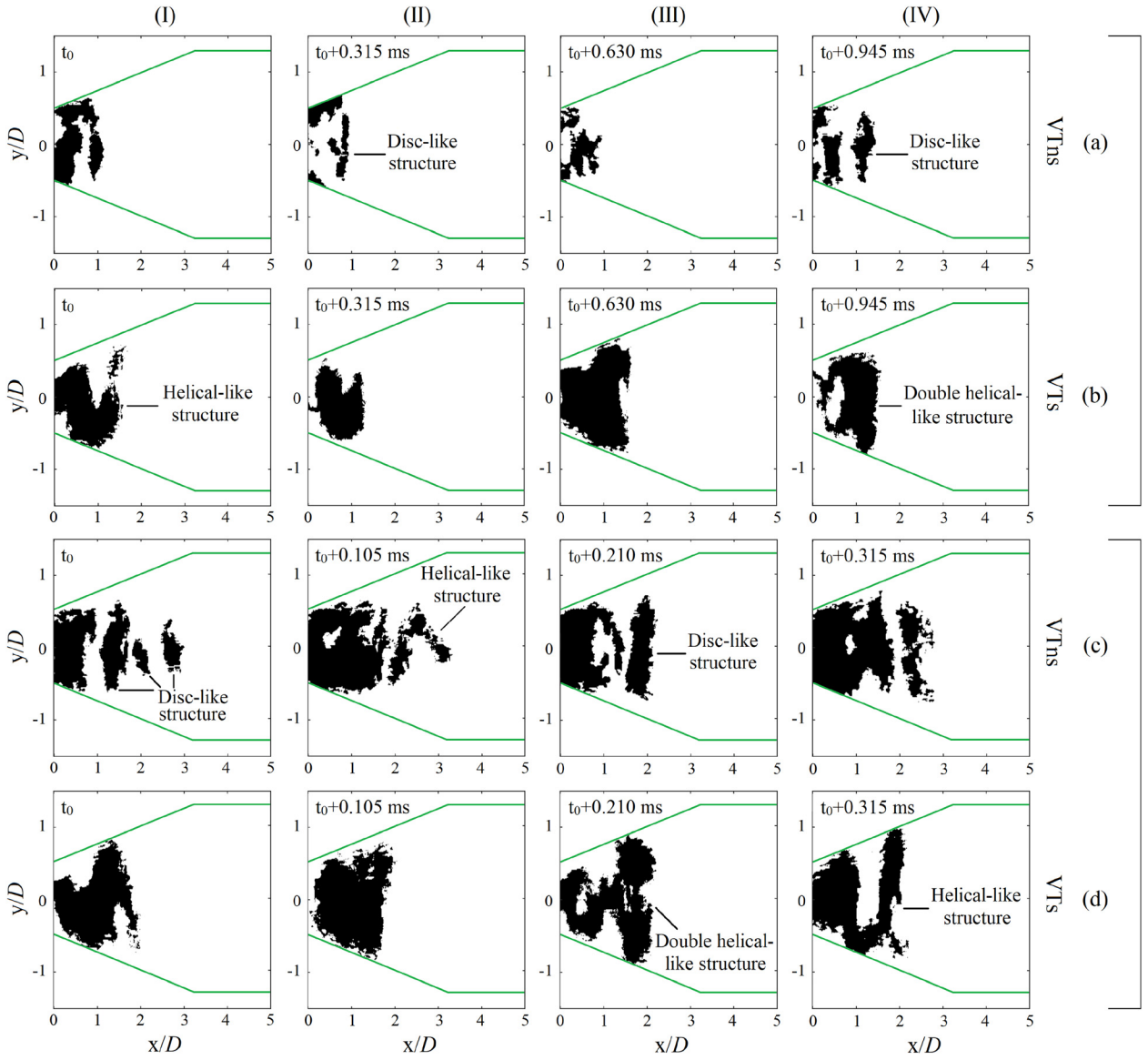

FIG. 3. Cavitation in VTns at (a) $\sigma = 1.4$ and (c) $\sigma = 1.3$ and VTs at (b) $\sigma = 1.4$ and (d) $\sigma = 1.3$.

consecutive turns of the helical structures. The results demonstrate that both the shedding length and the pitch increase with decreasing cavitation number. This indicates that disk-like structures in VTns persist for longer distances at low cavitation numbers, while helical structures are more open at high water flow rates.

Here, the spatiotemporal characteristics of coherent motions are evaluated by utilizing SPOD, and the results are presented in Fig. 6. In this figure, the first two most energetic modes of coherent motions are shown alongside their frequencies and energy percentages annotated in the frames. The results show that the first most energetic modes are asymmetric in the streamwise direction (x axis), while they are symmetric in the spanwise direction (y axis). In the VTns venturi tube, this mode resembles the disk-like structures observed in Fig. 3. However, the first mode in the VTs tube takes the shape of an arc, with both sides reaching the wall. This pattern represents the axial motion of helical-like and double helical-like structures. Additionally, unlike VTns, the second mode in the swirled case is asymmetric in both x and y directions. This indicates that the second most energetic modes in the VTns venturi tube correspond to the small-scale high-frequency structures. In contrast, the second most energetic modes in the VTs case represent azimuthal motions of helical-like and double helical-like structures.

Figure 6 also shows that the frequency of coherent motions is consistently higher in the VTns than in the VTs venturi tube for different modes and cavitation numbers. Furthermore, comparing the energy percentages of the modes shows that the mechanism exciting

22 April 2026 09:41:02

© Author(s) 2026

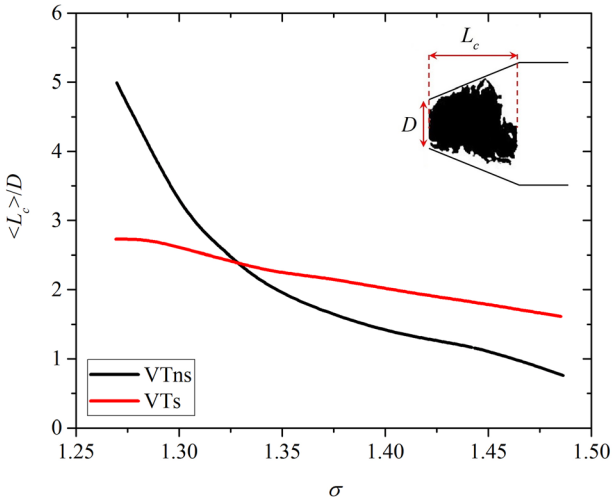

FIG. 4. Averaged value of cavitating length in VTns and VTs as a function of the cavitation number.

the first mode is substantially stronger in the VTs venturi tube than that in the VTns, whereas the second mode receives more energy in the VTns venturi tube than the VTs. This indicates that introducing swirl to cavitating flows shifts the dynamics toward slowly evolving coherent motions. The results also show that decreasing the cavitation number reduces the frequency of coherent motions in both cases. This is an interesting observation because decreasing the cavitation number is accompanied by higher flow velocity, which should presumably shift the flow dynamics toward fast-evolving motions. However, as shown in Fig. 5, reducing σ increases the characteristic length of coherent structures in both VTns and VTs cases, with more pronounced changes in VTns. This, in turn, suppresses the effects of increases in the advection velocity on the frequency.

B. Microscale characteristics

This section presents microscale characteristics of cavitating flows in VTns and VTs venturi tubes. Section III A (Fig. 3) shows that the overall shape of dominant flow structures of interest remains qualitatively similar at different cavitation numbers. Therefore, considering the time constraints for using the SPB/SFX x-ray instrument of the European XFEL, we chose to characterize the microscale features of the venturi tubes at $\sigma = 1.4$. The experiments were performed at different spatial locations of the venturi tubes by repositioning the megahertz-rate camera and the venturi tubes relative to the x-ray beam. Here, we present experimental data obtained using 10× and 5× magnifications in the VTns and VTs venturi tubes, respectively, ensuring optimal resolution for resolving the features of interest.

Figure 7 shows the general features of cavitation in the VTns venturi tube. The grayscale contours show the image intensity normalized by the maximum value in each frame. Moreover, the venturi wall is highlighted in green. Results indicate that cavitation in VTns involves deterministic features associated with the attached sheet cavitation near the throat. Such structures evolve into more complex features further downstream, followed by detachment of vapor structures at $t = t_0 + 4.4\,\mu$s, forming cloud cavitation. According to previous studies, hydrodynamic sheet cavitation forms when the flow passes a wall near low-pressure points, while trapping microbubbles as nuclei for inception.[107–109] Our experiments reveal an additional mechanism for sheet cavitation formation in the VTns venturi tube. Figure 8 shows the temporal evolution of this mechanism in a magnified view of the flow near the VTns wall. At $t = t_0$, the flow contains no cavitating regions or microbubbles, at least not at dimensions resolvable with the current high-resolution imaging technique. In the following sequences of images, a sheet cavitation propagates upstream and grows until it forms a stable sheet cavitation sustaining itself at $t = t_0 + 37.2\,\mu$s. Tracking similar features in 18 sets of experiments shows that the averaged velocity of such motion is approximately 10% of the throat velocity. This suggests that cavitating regions formed downstream

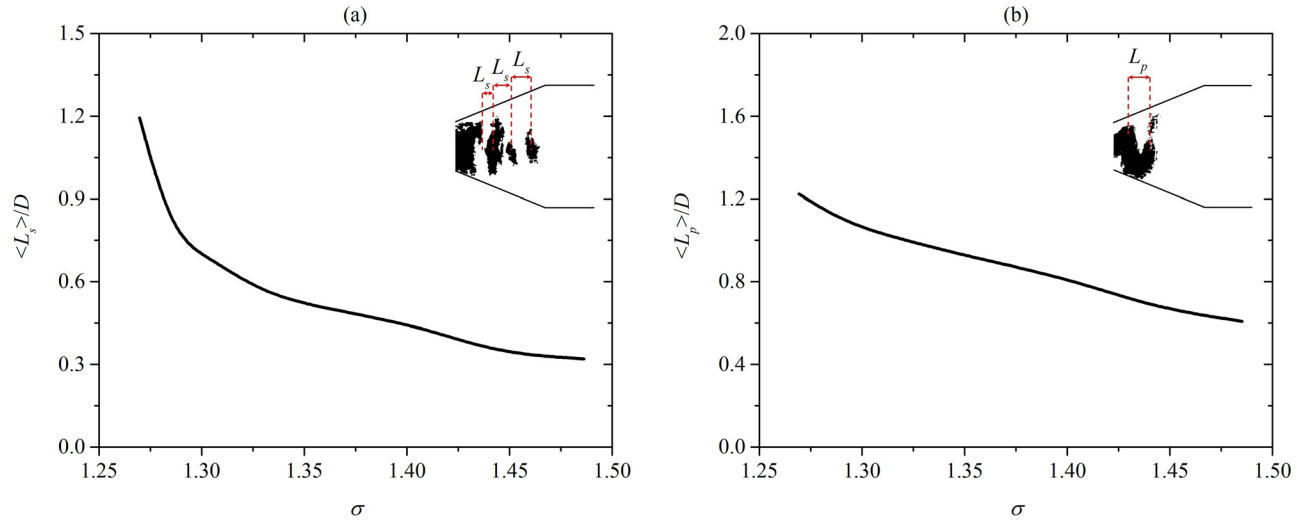

FIG. 5. Averaged value of (a) cavitation shedding length and (b) pitch as a function of the cavitation number.

22 April 2026 09:41:02

© Author(s) 2026

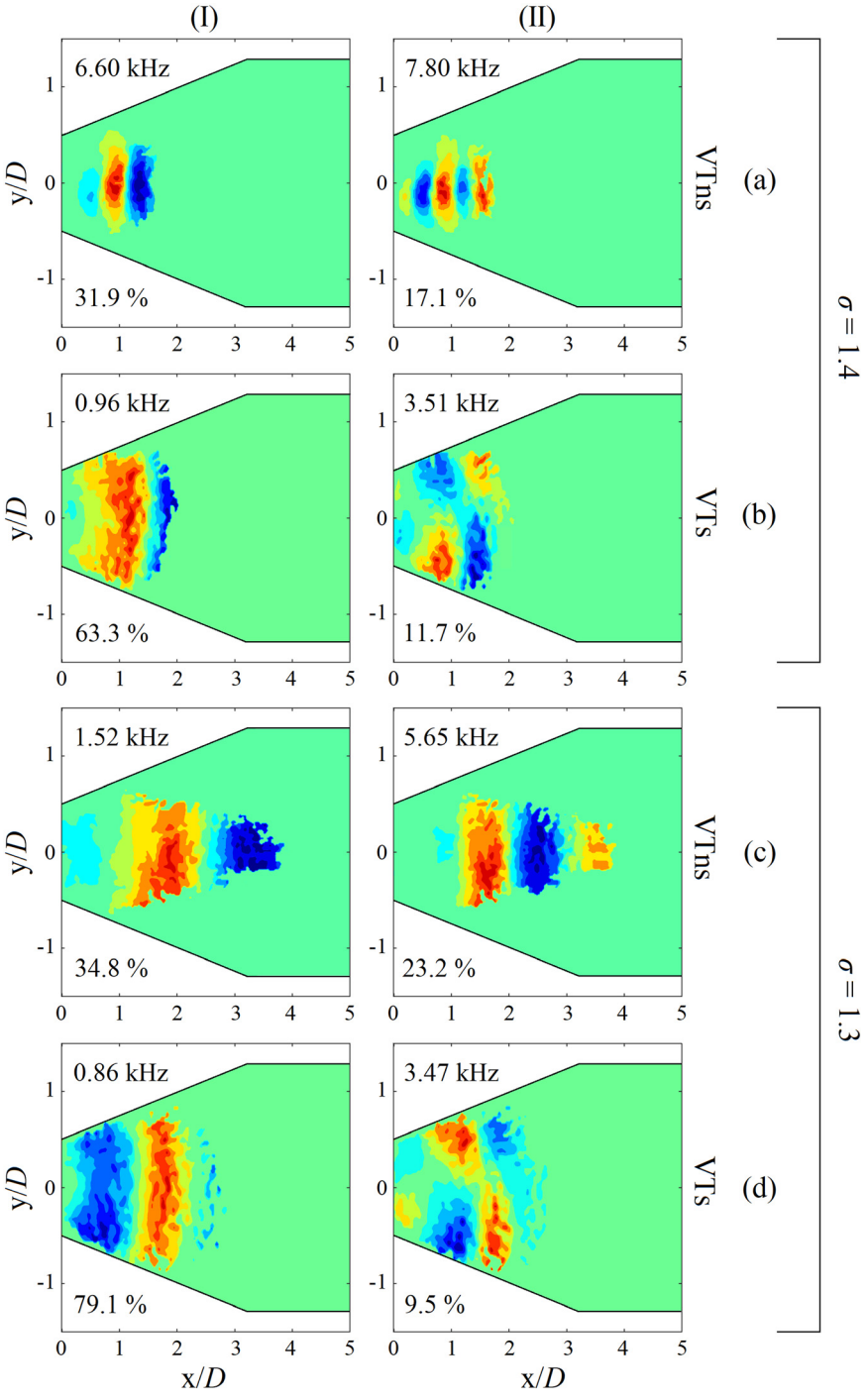

FIG. 6. Spatial distributions of the (I) first and (II) second most energetic modes of coherent structures in VTns for (a) $\sigma = 1.4$ and (c) $\sigma = 1.3$ and VTs for (b) $\sigma = 1.4$ and (d) $\sigma = 1.3$. The frequency and energy percentage of the modes are annotated in each frame.

propagate through the low-velocity regions near the wall, feeding the formation of sheet cavitation near the throat.

Figure 9 demonstrates the general features of cavitation in the VTs venturi tube. Here, the grayscale contours show the image intensity normalized by the maximum value in each frame and the bluff body is highlighted in green. The results show that the cavitating region is usually attached to the bluff body, forming a sheet of bubbles. However, this sheet quickly converts into a cloud cavitation, moving with the swirling motion. During $t_0 < t < t_0 + 8.8\,\mu$s, the cloud takes a helical-like structure, followed by a more symmetrical cloud with respect to the y axis at $t_0 + 44.2\,\mu$s. The cavitation also exhibits twofold features, as shown in Fig. 9 at $t_0 + 0.7$ s,

22 April 2026 09:41:02

© Author(s) 2026

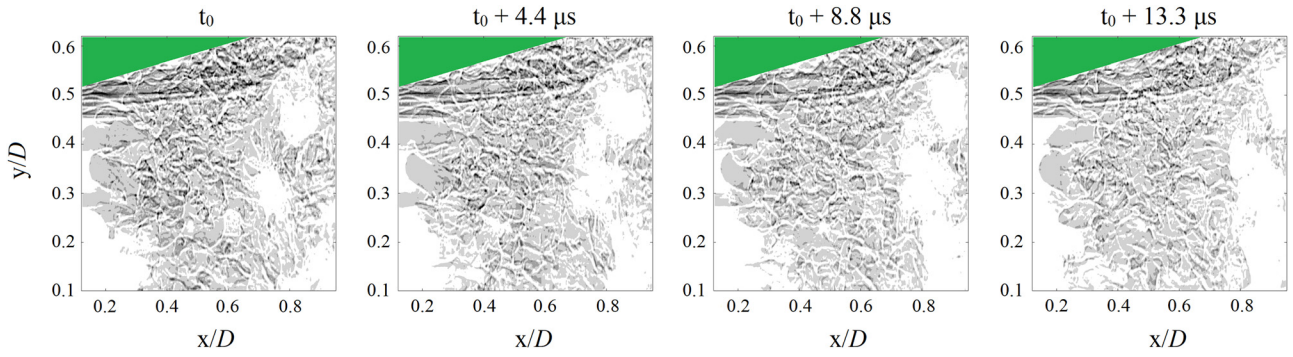

FIG. 7. Cavitation in the VTns venturi tube. The grayscale contour ranges from 0 (white) to 1 (black).

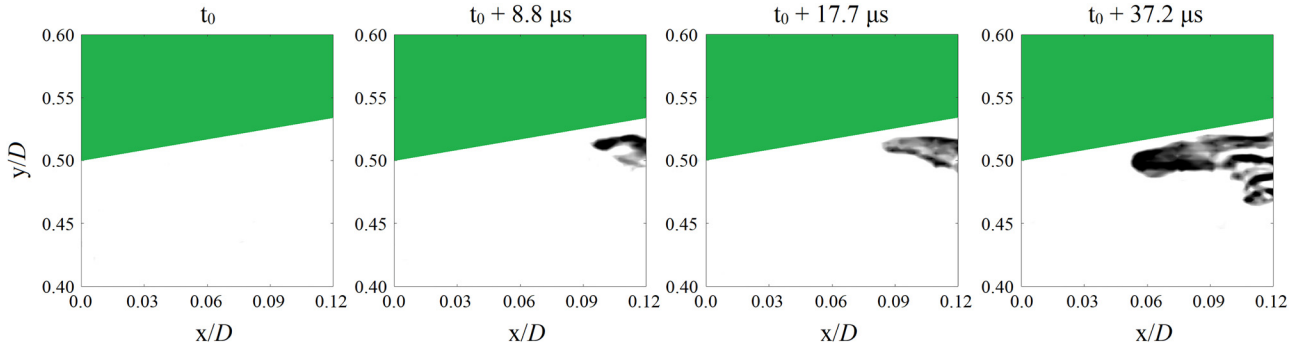

FIG. 8. An upstream-propagating cavity along the wall in the VTns venturi tube. The grayscale contour is limited to 0 (white) to 0.5 (black) to enhance the visibility of the bubbles, where cavities appear in shades of gray and black.

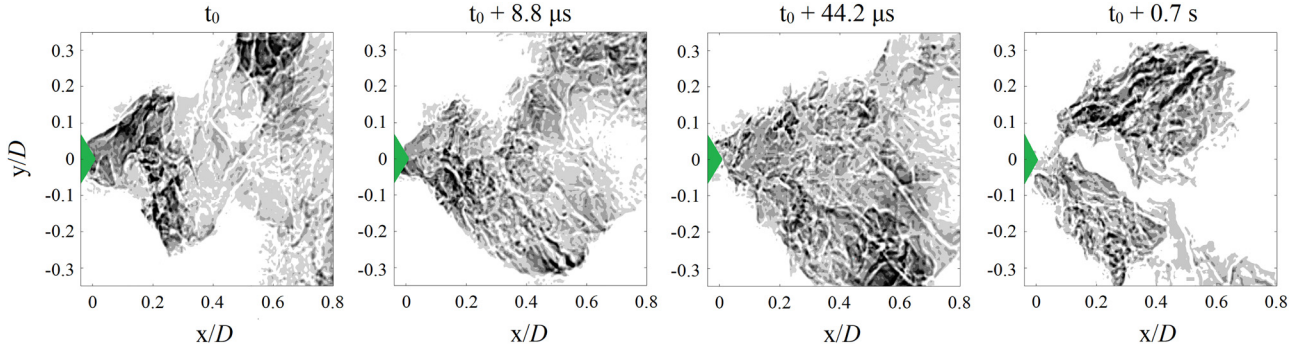

FIG. 9. Cavitation in the VTs venturi tube. The grayscale contour ranges from 0 (white) to 1 (black).

which was taken from another train of images following the present set of images.

As detailed in Sec. III A, helical-like structures are well known to be due to the combination of Kelvin–Helmholtz and centrifugal instabilities. However, twofold features are rarely observed in swirling cavitation flows. Figure 10 illustrates one of the mechanisms driving the formation of double helical-like structures. Further details of this mechanism are provided in the video file included as the supplementary material. At $t = t_0$, the flow contains a small cavitating region near a helical-like structure. This pocket of vapor bubbles gradually rotates and expands over time. To visualize the rotation, a specific point on this pocket, labeled A, is tracked in each frame to illustrate the rotation. This pocket likely formed in the low-pressure region at the core of a vortex, merges with the helical-like structure at $t = t_0 + 13.3\ \mu$s, and forms a twofold structure at $t = t_0 + 18.6\ \mu$s.

Figure 11 shows the microscale characteristics of coherent motions in VTns and VTs venturi tubes obtained using SPOD. Here, the first two most energetic modes of coherent motions are presented

22 April 2026 09:41:02

© Author(s) 2026

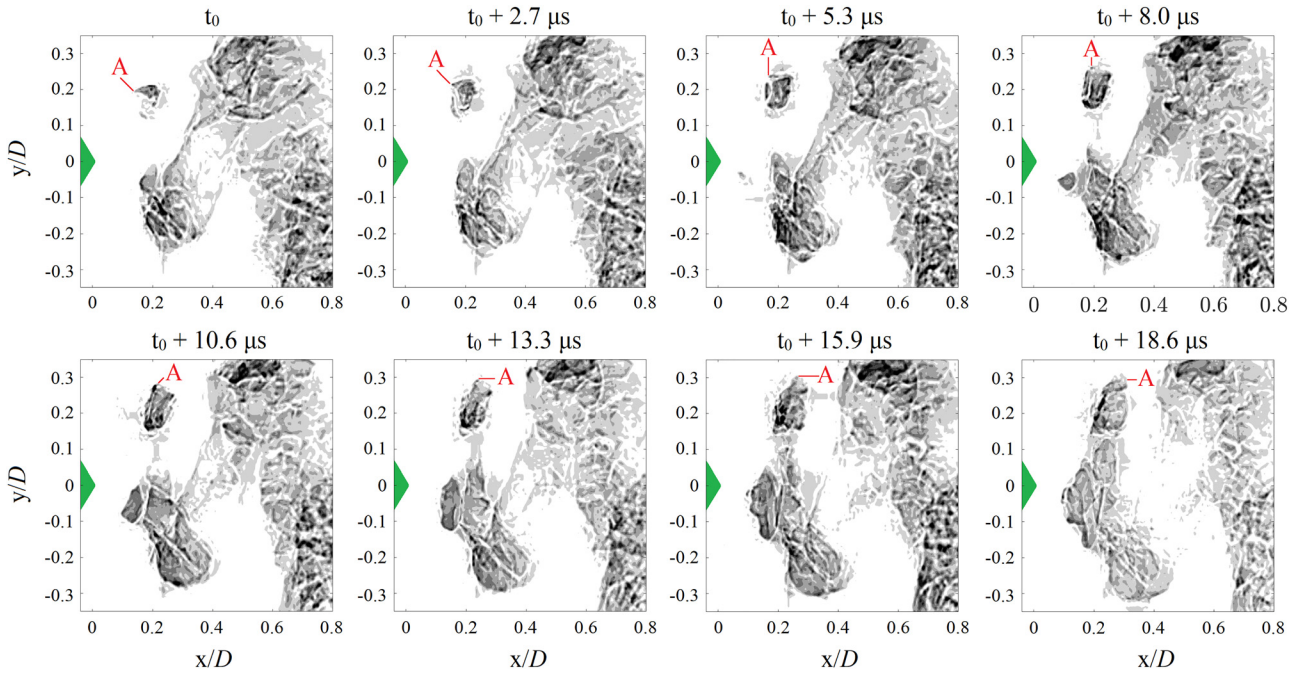

FIG. 10. Formation of a double helical-like structure in the VTs venturi tube. The grayscale contour ranges from 0 (white) to 1 (black).

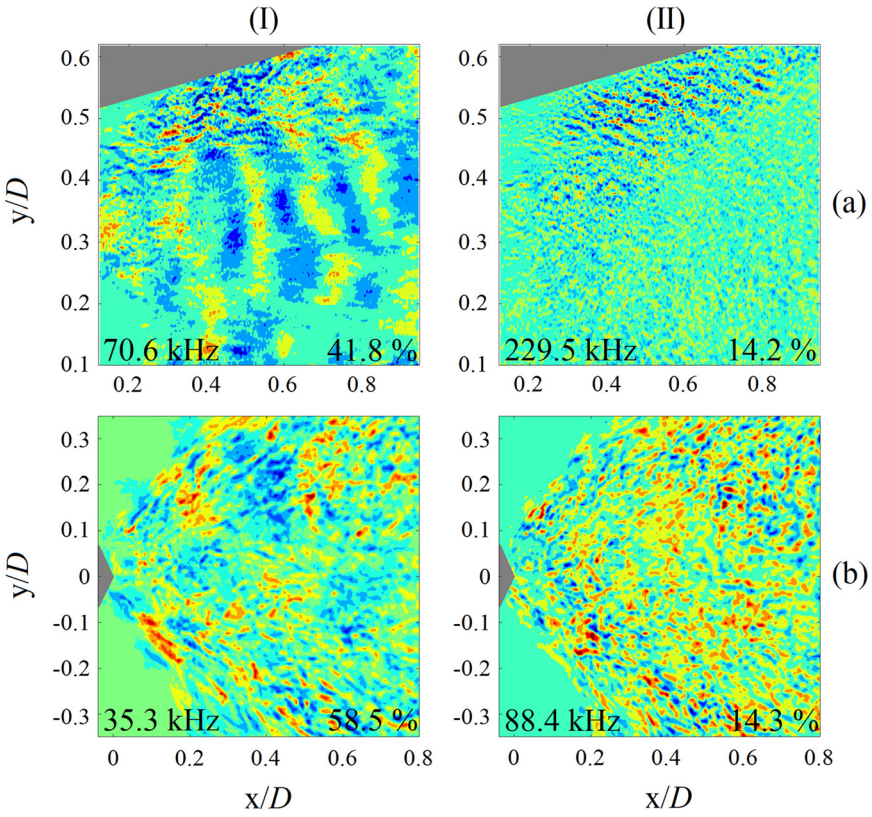

FIG. 11. Spatial distributions of the (I) first and (II) second most energetic modes of coherent structures in the (a) VTns and (b) VTs venturi tubes. The frequency and energy percentage of the modes are annotated in each frame.

22 April 2026 09:41:02

© Author(s) 2026

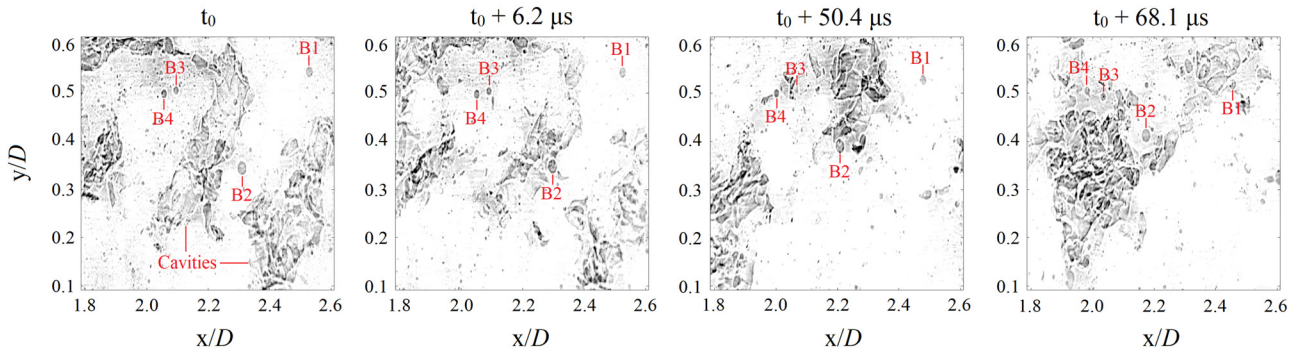

FIG. 12. Microbubbles in a cavitating flow. The grayscale contour is limited to 0.1 (white) to 0.5 (black) to enhance the visibility of the bubbles, where cavities and microbubbles appear in shades of gray and black.

alongside their frequencies and energy percentages, annotated in the figures. The main microscale features of coherent motions in the VTns venturi tube are similar to its mesoscale characteristics highlighted in Fig. 6—the first most energetic mode is asymmetric and symmetric in the streamwise and spanwise directions, respectively, which are associated with the sheet cavitation shedding in this venturi tube. The second most energetic mode in the VTns venturi tube corresponds to the vortical structures in shear layers between the sheet cavitation and the bulk flow. These structures are visible only near the upper wall region of the venturi tube, where the direct imaging technique is capable of resolving three-dimensional motions, such as those in the radial direction. Figure 11(b) illustrates that the first most energetic mode in the VTs venturi tube exhibits an asymmetric pattern in the streamwise direction and is also asymmetric with respect to the bluff body's cone axis. This indicates that the most energetic mode in the swirled case comprises both axial and azimuthal motions of the helical- and double helical-like structures. The second most energetic mode in the VTs venturi tube is associated with small-scale high-frequency coherent motions. A comparison of the frequencies of these modes shows that, in agreement with Fig. 6, the coherent motions in the VTns venturi tube have significantly higher frequency contents than those in the VTs venturi. However, the frequencies of microscale structures are at least an order of magnitude higher than those of mesoscale structures. This finding highlights that SPOD based on shadowgraph imaging does not fully reflect the physical features of cavitation in venturi tubes.

It is known that microbubbles have a significant influence on hydrodynamic cavitation features. These bubbles can work as nuclei to initiate cavitation.[108,110] Furthermore, mesoscale analyses of cavitation seeded by microbubbles have demonstrated that bubbles can break down the coherency of cavitation by generating dispersed cavities.[111] Proximity of either air or vapor bubbles to vapor cavities can also significantly alter the cavitation collapse pressure.[29,87,112] We used the high-resolution phase-contrast x-ray imaging technique to resolve and track these microbubbles in the flow. These analyses show that following the cavitation collapses, the images exhibit numerous spherical-shaped bubbles generated downstream of the throat in both VTns and VTs venturi tubes. Some of these bubbles are shown in Fig. 12, labeled as B1 to B4, alongside the vapor cavities. Tracking microbubbles and large-scale cavities over time, e.g., those shown in Fig. 12 at t_0, reveals that microbubbles retain their shape and size for a longer period than cavities. To quantify the specifications of these bubbles, Fig. 13 shows the velocity magnitude of these bubbles, $|U|$, normalized by the magnitude of velocity at the throat, $|U_t|$, as a function of their radius, R_b. The bubbles are also color-coded based on the percentage changes in their radius, ΔR_b, over a sequence of images captured within 113 μs. Considering the spatial resolution of the imaging technique, we could detect bubbles with a radius greater than 6 μm. Moreover, our investigations show that the flow rarely contains bubbles larger than 19 μm in radius. Figure 13 reveals that the velocity magnitude of the microbubbles is less than 20% of the magnitude of the flow velocity at the throat, and their sizes change by less than 33% in a sequence of 124 images. This suggests that such bubbles likely contain a noticeable amount of non-condensable gases.

Our investigations also showed that these microbubbles could seed the cavitation. Figure 14 illustrates an example of this process by plotting the motion trajectory of a microbubble. Here, the bubble is colored by its velocity, calculated by tracking its center in two consecutive images. According to Fig. 14, the bubble retains its shape and size during $t_0 < t < t_0 + 52.2\,\mu$s, while moving relatively slowly in the streamwise direction. At $t = t_0 + 81.4\,\mu$s, it evolves into a flat-like structure, while its velocity increases to 0.35% of the throat velocity.

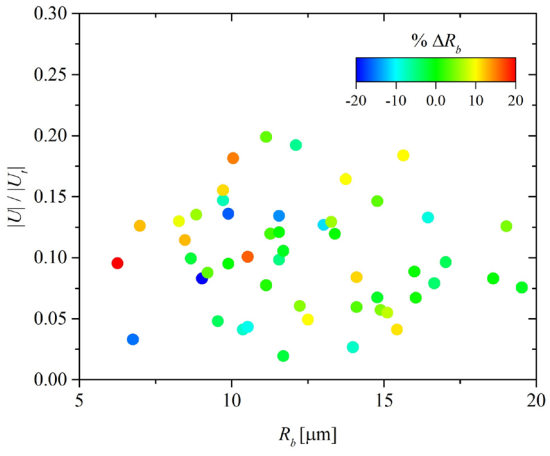

FIG. 13. The velocity magnitude of microbubbles as a function of the bubble radius, color-coded by the percentage changes in their radius over 113 μs.

22 April 2026 09:41:02

© Author(s) 2026

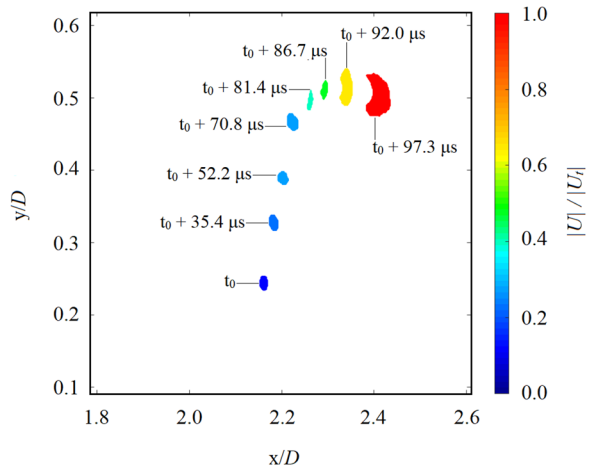

FIG. 14. Motion trajectory of microbubble evolving into cavitation bubble.

Following this, it enlarges and moves significantly faster in the flow until it turns into a cavitating bubble at $t_0 + 97.3\ \mu s$. This trend indicates that microbubbles moving within low-velocity regions of the flow rarely trigger cavitation. However, they work as nuclei for cavitation as they are involved in high-velocity motions. We observed the bubble-to-cavitation transition for different sizes of bubbles. Nevertheless, additional investigations are necessary to establish the effects of bubble size and distribution, as well as flow conditions, on the bubble-to-cavitation transition, as the present study was restricted to a fixed operating condition.

The results presented in this paper were obtained for a typical venturi tube used in applications involving hydrodynamic cavitation. However, results should be interpreted with care for venturi tubes with different divergence angles and operating conditions. An increase in the divergence angle is expected to result in the dominance of the cloud cavitation regime, and the flow Reynolds number can significantly affect the frequency of the coherent motions.

IV. CONCLUSIONS

In this paper, we employed shadowgraph imaging at the University of Oxford and high-speed phase-contrast x-ray imaging at the European XFEL to evaluate mesoscale and microscale characteristics of hydrodynamic cavitation and the effects of swirl on them.

This study demonstrated that introducing swirl significantly reduces the hydraulic power to initiate cavitation, with potential implications for improving the efficiency of processes that rely on hydrodynamic cavitation. Investigations indicated that the non-swirl flow is dominated by sheet cavitation, evolving into cloud cavitation as the flow moves downstream. Cavitation shedding in non-swirled flow involves disk-like structures. Introducing swirl increases the inception cavitation number and shifts the cavitation toward a more stable cloud regime when compared to non-swirled flow. Swirl also reshapes the coherent motions into low-frequency helical-like and double helical-like structures. Results also indicated that reducing the cavitation number increases the shedding length and pitch of coherent structures while decreasing their frequencies. Furthermore, microscale measurements highlighted microscale bubbles moving randomly in the flow field downstream of the venturi tubes. These bubbles maintain their shapes as they move within the low-velocity regions and can trigger cavitation when they are involved in high-velocity flow motions.

SUPPLEMENTARY MATERIAL

See the supplementary material for a video showing the formation of a double helical-like structure under the conditions described in Sec. III B and Fig. 10.

ACKNOWLEDGMENTS

This study, as a part of the MHz-TOMOSCOPY project, was funded by the HORIZON-EIC-2021-PATHFINDEROPEN-01-01 call, Grant Agreement No. 101046448; EuXFEL R&D "MHz X-ray microscopy: From demonstration to method," 2020–2022; Bundesministerium für Bildung und Forschung (BMBF) (No. 05K18XXA); and Vetenskapsrådet (VR) (No. 2017-06719). We thank the EuXFEL in Schenefeld, Germany, for the provision of XFEL beam time at the Scientific Instrument SPB/SFX under Proposal No. 7156 and thank the staff for their assistance. P.V. and J.C.P.K. thank Thomas Dietze for technical support. The hydraulic loop of the experimental setup was provided by the Department of Finemechanics, Tohoku University.

AUTHOR DECLARATIONS

Conflict of Interest

The authors have no conflicts to disclose.

Author Contributions

M. Shahsavari: Conceptualization (equal); Data curation (equal); Formal analysis (equal); Investigation (equal); Methodology (equal); Project administration (equal); Software (equal); Validation (equal); Visualization (equal); Writing – original draft (equal); Writing – review & editing (equal). **D. Eakins:** Conceptualization (equal); Data curation (equal); Formal analysis (equal); Funding acquisition (equal); Investigation (equal); Methodology (equal); Project administration (equal); Resources (equal); Software (equal); Supervision (equal); Validation (equal); Visualization (equal); Writing – original draft (equal); Writing – review & editing (equal). **P. Vagovič:** Conceptualization (equal); Data curation (equal); Funding acquisition (lead); Investigation (equal); Methodology (equal); Project administration (equal); Resources (equal); Validation (supporting); Visualization (supporting); Writing – review & editing (supporting). **H. Soyama:** Conceptualization (equal); Methodology (supporting); Writing – review & editing (supporting). **J. C. P. Koliyadu:** Funding acquisition (supporting); Investigation (supporting); Methodology (supporting); Resources (supporting); Writing – review & editing (supporting). **T. Sato:** Funding acquisition (supporting); Investigation (supporting); Methodology (supporting); Resources (supporting); Writing – review & editing (supporting). **R. Graceffa:** Funding acquisition (supporting); Investigation (supporting); Resources (supporting); Writing – review & editing (supporting). **A. Mazzolari:** Investigation (supporting); Resources (supporting); Writing – review & editing (supporting). **S. Birnsteinova:** Visualization (supporting); Writing – review & editing (supporting). **D. Mosko:** Funding acquisition (supporting); Investigation (supporting); Writing – review & editing (supporting). **P. Szeles:** Investigation (supporting); Writing – review & editing (supporting). **J. Uličný:** Funding acquisition (supporting); Investigation

22 April 2026 09:41:02

© Author(s) 2026

(supporting); Resources (supporting); Writing – review & editing (supporting). **W. Yashiro:** Investigation (supporting); Writing – review & editing (supporting). **A. Meents:** Funding acquisition (supporting); Investigation (supporting); Resources (supporting); Writing – review & editing (supporting).

DATA AVAILABILITY

The data that support the findings of this study are available from the corresponding author upon reasonable request.

APPENDIX: MEASUREMENT UNCERTAINTY

The standard uncertainty of the cavitation number, u_σ, and the relative standard uncertainty of hydraulic power, u_{P_h}/P_h (%), were evaluated using the following equations derived from the first-order uncertainty propagation method:

$$u_\sigma = \left[\left(\frac{\partial\sigma}{\partial p_1}\right)^2 u_{p_1}^2 + \left(\frac{\partial\sigma}{\partial p_2}\right)^2 u_{p_2}^2 + \left(\frac{\partial\sigma}{\partial p_{vap}}\right)^2 u_{p_{vap}}^2\right]^{1/2}, \quad \text{(A1)}$$

$$\frac{u_{P_h}}{P_h} = 100 \times \left[\left(\frac{\partial P_h}{\partial \dot{Q}}\right)^2 u_{\dot{Q}}^2 + \left(\frac{\partial P_h}{\partial p_i}\right)^2 u_{p_i}^2 + \left(\frac{\partial P_h}{\partial p_e}\right)^2 u_{p_e}^2\right]^{1/2} \times P_h^{-1}, \quad \text{(A2)}$$

where the uncertainties of pressure measurements upstream and downstream of venturi tubes, u_{p_1} and u_{p_2}, and pressure measurements upstream and downstream of the pump, u_{p_i} and u_{p_e}, were evaluated as standard uncertainties assuming rectangular distributions using

$$u_{p_j} = \frac{a \times FS}{\sqrt{3}}, \quad j = 1, 2, i, e. \quad \text{(A3)}$$

In Eq. (A3), a and FD are the pressure transmitter accuracy and full-scale range, respectively. Additionally, the uncertainty of volume flow rate measurement, $u_{\dot{Q}}$, was estimated using

$$u_{\dot{Q}} = \frac{1}{\sqrt{3}}\left[\left(a \times \dot{Q}\right)^2 + \left(r \times \dot{Q}\right)^2\right]^{1/2}, \quad \text{(A4)}$$

where $\dot{Q}$ is the measured volume flow rate and r is the sensor repeatability. In this study, the vapor pressure was obtained from the NIST database based on the measured temperature, T. Therefore, the uncertainty of the vapor pressure, p_{vap}, was estimated using

$$u_{p_{vap}} = \left|\frac{p_{vap}(T + \Delta T) - p_{vap}(T - \Delta T)}{2\Delta T}\right| u_T, \quad \text{(A5)}$$

where ΔT is 0.1 °C and u_T is the thermocouple uncertainty, which is $\frac{a}{\sqrt{3}}$ °C.

REFERENCES

[1] C. E. Brennen, *Cavitation and Bubble Dynamics* (Oxford University Press, 1995).
[2] D. Ao, Y. Li, C. Liu, and Z. Wang, "Study on cavitation flow characteristics of orifice plate-elbow structure in liquefied natural gas receiving station," Phys. Fluids **37**, 096115 (2025).
[3] W. Bergwerk, "Flow pattern in diesel nozzle spray holes," Proc. Inst. Mech. Eng. **173**, 655–660 (1959).
[4] W. H. Nurick, "Orifice cavitation and its effect on spray mixing," J. Fluids Eng. **98**, 681–687 (1976).
[5] T. Trummler, S. J. Schmidt, and N. A. Adams, "Investigation of condensation shocks and re-entrant jet dynamics in a cavitating nozzle flow by large-eddy simulation," Int. J. Multiphase Flow **125**, 103215 (2020).
[6] J. J. Zhao, L. H. Meng, H. T. Zhang, M. Yu, Z. Lin, and G. Zhang, "A review of prediction methods of cavitation erosion," Phys. Fluids **37**, 111301 (2025).
[7] Z. Wang, X. Li, Z. Zhu, X. Li, W. Zhang, and L. Li, "Cavitation erosion in venturi pipe and erosion optimization of four-stage pump," Phys. Fluids **37**, 092118 (2025).
[8] H. Soyama, "Comparison between the improvements made to the fatigue strength of stainless steel by cavitation peening, water jet peening, shot peening and laser peening," J. Mater. Process. Technol. **269**, 65–78 (2019).
[9] H. Soyama and A. M. Korsunsky, "A critical comparative review of cavitation peening and other surface peening methods," J. Mater. Process. Technol. **305**, 117586 (2022).
[10] H. Soyama and Y. Iga, "Laser cavitation peening: A review," Appl. Sci. **13**, 6702 (2023).
[11] H. Soyama, K. L. Wong, D. Eakins, and A. M. Korsunsky, "The effects of submerged laser peening, cavitation peening, and shot peening on the improvement of the torsional fatigue strength of powder bed fused Ti6A14V produced through laser sintering," Int. J. Fatigue **185**, 108348 (2024).
[12] C. D. Ohl, M. Arora, R. Dijkink, V. Janve, and D. Lohse, "Surface cleaning from laser-induced cavitation bubbles," Appl. Phys. Lett. **89**, 074102 (2006).
[13] P. Cui, A. M. Zhang, S. P. Wang, and Y. L. Liu, "Experimental study on interaction, shock wave emission and ice breaking of two collapsing bubbles," J. Fluid Mech. **897**, A25 (2020).
[14] M. Shan, Y. Zha, Y. Yang, C. Yang, C. Yin, and Q. Han, "Morphological characteristics and cleaning effects of collapsing cavitation bubble in fractal cracks," Phys. Fluids **36**, 063337 (2024).
[15] M. Zupanc, T. Kosjek, M. Petkovšek, M. Dular, B. Kompare, B. Širok, Z. Blažeka, and E. Heath, "Removal of pharmaceuticals from wastewater by biological processes," Ultrason. Sonochem. **20**, 1104–1112 (2013).
[16] Z. Pandur, J. Zevnik, D. Podbevsek, B. Stojkovic, D. Stopar, and M. Dular, "Water treatment by cavitation: Understanding it at a single bubble-bacterial cell level," Water Res. **236**, 119956 (2023).
[17] A. Vijayan and P. P. Kumar, "Characterization of cavitation zone in cavitating venturi flows: Challenges and road ahead," Phys. Fluids **35**, 111301 (2023).
[18] S. K. Singh, P. S. Duth, P. Kumar, E. Kadivar, and O. el Moctar, "Experimental investigation of the cavitation control in a convergent–divergent nozzle using air injection," Phys. Fluids **36**, 113348 (2024).
[19] S. Tebyani, E. Toyran, F. R. Talabazar, M. Ghorbani, and A. Koşar, "Acoustic characterization of cavitating flows in a microfluidic venturi reactor," Phys. Fluids **37**, 082142 (2025).
[20] H. Zhang, Z. Zuo, K. A. Mørch, and S. Liu, "Thermodynamic effects on venturi cavitation characteristics," Phys. Fluids **31**, 097107 (2019).
[21] M. Ge, M. Petkovšek, G. Zhang, D. Jacobs, and O. Coutier-Delgosha, "Cavitation dynamics and thermodynamic effects at elevated temperatures in a small venturi channel," Int. J. Heat Mass Transf. **170**, 120970 (2021).
[22] A. Wei, L. Yu, R. Gao, W. Zhang, and X. Zhang, "Unsteady cloud cavitation mechanisms of liquid nitrogen in convergent–divergent nozzle," Phys. Fluids **33**, 092116 (2021).
[23] A. Sou, B. Biçer, and A. Tomiyama, "Numerical simulation of incipient cavitation flow in a nozzle of fuel injector," Comput. Fluids **103**, 42–48 (2014).
[24] B. Charrière and E. Goncalves, "Numerical investigation of periodic cavitation shedding in a venturi," Int. J. Heat Fluid Flow **64**, 41–54 (2017).
[25] S. Xu, X. Long, J. Wang, H. Cheng, and Z. Zhang, "Experiment on flow dynamics and cavitation structure in an axisymmetric venturi tube based on x–t diagrams and proper orthogonal decomposition," Exp. Therm. Fluid Sci. **136**, 110648 (2022).
[26] R. E. A. Arndt, "Cavitation in vortical flows," Annu. Rev. Fluid Mech. **34**, 143–175 (2002).
[27] S. Gopalan and J. Katz, "Flow structure and modeling issues in the closure region of attached cavitation," Phys. Fluids **12**, 895–911 (2000).

22 April 2026 09:41:02

© Author(s) 2026

[28]C. Gouin, C. Junqueira-Junior, E. D. Silva, and J. Robinet, "Numerical investigation of three-dimensional partial cavitation in a venturi geometry," Phys. Fluids **33**, 063312 (2021).
[29]O. Ram, K. Agarwal, and J. Katz, "On the mechanisms that sustain the inception of attached cavitation," J. Fluid Mech. **901**, A25 (2020).
[30]C. Wang, P. Wang, W. Zhao, and X. Han, "Effects of solid particle concentration on solid particle-water cavitating jet evolution in venturi tube," Phys. Fluids **37**, 103306 (2025).
[31]R. T. Knapp, "Recent investigations of the mechanics of cavitation and cavitation damage," Trans. ASME **77**, 1045–1054 (1955).
[32]G. E. Reisman, Y.-C. Wang, and C. E. Brennen, "Observations of shock waves in cloud cavitation," J. Fluid Mech. **355**, 255–283 (1998).
[33]M. Callenaere, J.-P. Franc, J.-M. Michel, and M. Riondet, "The cavitation instability induced by the development of a re-entrant jet," J. Fluid Mech. **444**, 223–256 (2001).
[34]G. Chen, G. Wang, C. Hu, B. Huang, Y. Gao, and M. Zhang, "Combined experimental and computational investigation of cavitation evolution and excited pressure fluctuation in a convergent–divergent channel," Int. J. Multiphase Flow **72**, 133–140 (2015).
[35]C. Stanley, T. Barber, and G. Rosengarten, "Re-entrant jet mechanism for periodic cavitation shedding in a cylindrical orifice," Int. J. Heat Fluid Flow **50**, 169–176 (2014).
[36]E.-J. Foeth, T. V. Terwisga, and C. V. Doorne, "On the collapse structure of an attached cavity on a three-dimensional hydrofoil," J. Fluids Eng. **130**, 071303 (2008).
[37]L. Yu, Q. Yi, H. Zhang, S. Liu, and Z. Zuo, "Cavitation in viscoelastic dilute polymer solutions through a venturi nozzle," Phys. Fluids **36**, 033359 (2024).
[38]R. Zhu, H. Zhu, X. Zhang, K. Deng, G. Ma, Z. Xie, and H. Chen, "Spatiotemporal cavitation dynamics in submerged cavitating jets: Influence of standoff distance," Phys. Fluids **37**, 123317 (2025).
[39]H. Ganesh, S. I. Mäkiharju, and S. E. Ceccio, "Bubbly shock propagation as a mechanism for sheet-to-cloud transition of partial cavities," J. Fluid Mech. **802**, 37–78 (2016).
[40]L. Li, X. Cheng, Z. Zhu, X. Sun, and X. Zhang, "Investigation of cavitation shedding mechanisms including reentrant jet and shock wave by Eulerian–Lagrangian multiscale simulation," Phys. Fluids **36**, 032126 (2024).
[41]B. Budich, S. J. Schmidt, and N. A. Adams, "Numerical simulation and analysis of condensation shocks in cavitating flow," J. Fluid Mech. **838**, 759–813 (2018).
[42]C. Wang, B. Huang, M. Zhang, G. Wang, Q. Wu, and D. Kong, "Effects of air injection on the characteristics of unsteady sheet/cloud cavitation shedding in the convergent–divergent channel," Int. J. Multiphase Flow **106**, 1–20 (2018).
[43]T. Chai, H. Cheng, L. Wang, Z. Zhang, Q. Hu, and X. Long, "Large eddy simulation of the cavitating flow in an annular jet pump with special emphasis on the cavitation–vortex interactions," Phys. Fluids **37**, 073359 (2025).
[44]W. Hou, S. Fan, X. Li, Y. Chen, X. Guo, and Z. Fang, "Mode decomposition of pressure effects on coherent structures in self-excited oscillating cavitation waterjets," Phys. Fluids **37**, 105126 (2025).
[45]L. Li, B. Shen, Z. Lin, Z. Zhu, B. Liu, M. Zhao, and X. Wang, "Investigation of cavitation jet erosion based on the Eulerian–Lagrangian approach coupled with dynamic mesh," Phys. Fluids **37**, 083419 (2025).
[46]C. Guo, S. Li, H. Wang, Z. Huang, G. Li, L. Xu, H. Li, and J. Li, "Geometric structural optimization of the diffusion section in the angular Helmholtz cavitation jet nozzle via Kriging–differential evolution model," Phys. Fluids **37**, 103315 (2025).
[47]R. Taghavi, "Cavitation inception in axisymmetric turbulent jets," Ph.D. thesis (University of Minnesota, 1985).
[48]R. Zhu, W. Xi, H. Zhu, X. Zhang, S. Pan, B. Li, and Z. Xie, "Flow field characteristics and three-dimensional coherent structures of free and impinging cavitating water jets: Effects of nozzle configuration," Phys. Fluids **37**, 083302 (2025).
[49]H. Chen, S. Liu, J. Zhang, and J. Xu, "An investigation of the cavitation and vibration phenomena in a cylindrical cyclone," Phys. Fluids **35**, 123302 (2023).
[50]Y. Zhang, X. Wan, X. Liu, B. Li, R. Han, Y. Xu, and H. Mei, "Flow field instability mechanism induced by cavitation inside the regulating valve," Phys. Fluids **37**, 085109 (2025).
[51]P. A. Brandner, B. W. Pearce, and K. de Graaf, "Cavitation about a jet in cross-flow," J. Fluid Mech. **768**, 141–174 (2015).
[52]H. Soyama, "Luminescence intensity of vortex cavitation in a venturi tube changing with cavitation number," Ultrason. Sonochem. **71**, 105389 (2021).
[53]A. Bhatt, H. Ganesh, and S. E. Ceccio, "Cavitating flow behind a backward facing step," Int. J. Multiphase Flow **139**, 103584 (2021).
[54]Q. Ye, Y. Wang, and X. Shao, "Dynamics of cavitating tip vortex," J. Fluid Mech. **967**, A30 (2023).
[55]J. J. Koncoski, X. I. A. Yang, R. F. Kunz, A. S. Nickels, D. W. Devilbiss, and J. R. Harris, "Experimental characterization of the flowfield and cavitation physics of a tip-loaded hydrofoil," Phys. Fluids **35**, 053336 (2023).
[56]S. Lak and R. K. Jaiman, "Suppressing tip vortex cavitation through passive deformation of a hydrofoil. I. bending," Phys. Fluids **37**, 083379 (2025).
[57]N. Qiu, Y. Ru, M. Li, H. Zhu, D. Xun, and F. Kong, "Control of leakage vortex cavitation in inducer of high-speed magnetic pump," Phys. Fluids **37**, 053339 (2025).
[58]M. Khozaei, A. Favrel, and K. Miyagawa, "Influence of swirling flow parameters on frequency response of a simplified draft-tube in presence of cavitation," Int. J. Heat Fluid Flow **98**, 109043 (2022).
[59]Z. Wang, D. Liu, B. Ji, and X. Luo, "Multiscale investigation of cavitation surge characteristics in the swirling flow using Eulerian–Lagrangian method," Ultrason. Sonochem. **120**, 107466 (2025).
[60]W. Wu, Y. Xu, Z. Yin, Y. Yan, J. Zhang, Z. Wang, and S. Li, "The flow characteristics of cavitation water jets with different nozzle structures," Phys. Fluids **37**, 025126 (2025).
[61]Z. Wang, Q. Zhao, Z. Yang, R. Liang, and Z. Li, "High-speed photography and particle image velocimetry of cavitation in a venturi tube," Phys. Fluids **36**, 045147 (2024).
[62]G. Yang, D. Zhang, X. Shen, Q. Pan, Q. Pang, and Q. Lu, "Investigation on flow instability in the hump region of the large vertical centrifugal pump under cavitation conditions based on proper orthogonal decomposition," Phys. Fluids **36**, 115134 (2024).
[63]G. Hatzissawidis, M. Sieber, K. Oberleithner, and P. Pelz, "Data-driven spatio-temporal analysis of cloud cavitation by means of spectral proper orthogonal decomposition," Exp. Fluids **66**, 104 (2025).
[64]J. L. Lumley, "Stochastic tools in turbulence," in *Applied Mathematics and Mechanics* (Academic Press, Inc., 1970).
[65]A. Yu, W. Feng, L. Li, W. Li, and D. Zhou, "Proper orthogonal decomposition analysis of the cavitating flow around a hydrofoil with an insight on the kinetic characteristics," Phys. Fluids **35**, 033309 (2023).
[66]Z. Fang, W. Hou, S. Fan, X. Guo, and Y. Chen, "Coherent structure analysis of cavitation waterjets using dynamic mode decomposition," Phys. Fluids **36**, 035114 (2024).
[67]T. Yin and G. Pavesi, "Interpreting proper orthogonal decomposition modes extracted from partial cavity oscillation," Phys. Fluids **37**, 013310 (2025).
[68]B. Hou, W. Hou, Q. Gao, Y. Wang, X. Guo, and Z. Fang, "The kinetic mechanism of vortex-cavitation interaction in dual-chamber self-excited oscillation waterjets," Phys. Fluids **37**, 025187 (2025).
[69]G. Berkooz, P. Holmes, and J. L. Lumley, "The proper orthogonal decomposition in the analysis of turbulent flows," Annu. Rev. Fluid Mech. **25**, 539–575 (1993).
[70]M. Sieber, C. Paschereit, and K. Oberleithner, "Spectral proper orthogonal decomposition," J. Fluid Mech. **792**, 798–828 (2016).
[71]S. Xu, J. Wang, H. Cheng, B. Ji, and X. Long, "Experimental study of the cavitation noise and vibration induced by the choked flow in a venturi reactor," Ultrason. Sonochem. **67**, 105183 (2020).
[72]A. Danlos, F. Ravelet, O. Coutier-Delgosha, and F. Bakir, "Cavitation regime detection through proper orthogonal decomposition: Dynamics analysis of the sheet cavity on a grooved convergent–divergent nozzle," Int. J. Heat Fluid Flow **47**, 9–20 (2014).
[73]S.-N. Wang, X.-D. Guo, N.-N. Liu, Z.-F. Meng, and L.-T. Liu, "Dynamics of spark-generated array bubbles near a free surface," Phys. Fluids **37**, 116129 (2025).
[74]Z. Zhao, J. Luo, W. Xu, J. Li, T. Qu, G. Fu, and Y. Ma, "Critical condition for inhibition effect of two cavitation bubbles with similar sizes near a rigid wall," Phys. Fluids **37**, 127110 (2025).
[75]H. Huang, Y. Zhang, Y. Jiang, X. Wu, and G. Li, "Experimental investigation of the cavitation bubble pulsation behavior under methane bubble interference," Phys. Fluids **37**, 127115 (2025).

22 April 2026 09:41:02

© Author(s) 2026

[76]S. Yang, W. Han, R. Li, X. Shen, H. Nan, and L. Zhu, "Weakening the synergistic strength of cavitation bubbles and wall particles," Phys. Fluids **37**, 083377 (2025).
[77]J. Yin, Y. Yu, Y. Zhang, L. Tian, M. Ma, R. Huang, and S. Zhang, "Collapse dynamics and jet transition in the interaction between a near-wall cavitation bubble and a spherical air bubble," Phys. Fluids **37**, 076115 (2025).
[78]H. Shi, X. Zhao, J. Chen, and X. Wang, "Effects of cavitation bubble dynamics near a free surface on gas layer stability and impact loading of biomimetic microstructured surfaces," Phys. Fluids **37**, 103311 (2025).
[79]Z. Wang, X. Wu, J. Hu, J. Wang, W. Wang, T. Ju, Y. Zhang, and Y. Zhang, "Investigation of the collapse behavior of a cavitation bubble near double cylinders within a narrow gap," Phys. Fluids **37**, 093341 (2025).
[80]J. Wang, B. Su, D. Shi, X. Bian, H. Zhang, and X. Cui, "Experimental investigation of secondary pulsation and load characteristics of spark-generated bubbles adjacent to a rigid horizontal wall," Phys. Fluids **37**, 096151 (2025).
[81]Y. Zhang, W. Liu, Q. Xu, T. Zhang, J. Shen, and Y. Zhang, "Investigation of the bubble splitting and jet dynamics near a corner within confined spaces," Phys. Fluids **37**, 103301 (2025).
[82]Y.-Q. Gao, Q. Zhong, Y.-L. Liu, S. Li, J.-F. Zhang, and A.-M. Zhang, "Study on the dynamics of underwater explosion bubbles near elastic–plastic cylindrical shells," Phys. Fluids **37**, 106113 (2025).
[83]S. Yang, W. Han, R. Li, X. Shen, and Q. Meng, "Experimental study of microjet impact mechanism under the action of vertical wall direction from single cavitation to triple cavitation bubble," Phys. Fluids **37**, 073349 (2025).
[84]Q. Dong, G. Liu, M. Guo, X. Li, M. Wang, and C. Xiong, "Dynamics of a single bubble collapse near a complex wall–ice boundary," Phys. Fluids **37**, 106129 (2025).
[85]Y. Wu, D. Zhao, L. Zhang, and Y. Li, "The collapse behavior and acoustic characteristics of bubble clusters with varied layers and fractions under the wall's shielding effect," Phys. Fluids **37**, 106105 (2025).
[86]N.-N. Liu, Y.-Y. Hu, P.-N. Sun, and Y.-X. Peng, "Interaction of underwater explosion bubble pair below a rigid wall," Phys. Fluids **37**, 126103 (2025).
[87]M. Shahsavari, D. Eakins, H. Soyama, T. Sato, J. Koliyadu, A. M. Korsunsky, and P. Vagovič, "On the collapse features of cavitation bubbles near a flat wall: Effects of pressure and tandem distribution," Phys. Fluids **37**, 093378 (2025).
[88]I. Xing, W. Han, R. Li, and Z. Yuan, "Investigation of shock wave loading characteristics in single/dual cavitation bubble collapse near rigid walls," Phys. Fluids **37**, 086133 (2025).
[89]A. Simpson and V. V. Ranade, "110th anniversary: Comparison of cavitation devices based on linear and swirling flows: Hydrodynamic characteristics," Ind. Eng. Chem. Res. **58**, 14488–14509 (2019).
[90]H. Shi, X. Wang, Q. Liu, and P. Nikrityuk, "The influence of inflow swirls on phases separation in a venturi tube," Sep. Purif. Technol. **281**, 119954 (2022).
[91]J. Kozák, P. Rudolf, M. Hudec, D. Štefan, and M. Forman, "Numerical and experimental investigation of the cavitating flow within venturi tube," J. Fluids Eng. **141**, 041101 (2019).
[92]P. Jain, V. Bhandari, K. Balapure, J. Jena, V. Ranade, and D. Killedar, "Hydrodynamic cavitation using vortex diode: An efficient approach for elimination of pathogenic bacteria from water," J. Environ. Manage. **242**, 210–219 (2019).
[93]G. Loraine, G. Chahine, C. T. Hsiao, J. Choi, and P. Aley, "Disinfection of gram-negative and gram-positive bacteria using Dynajets® hydrodynamic cavitating jets," Ultrason. Sonochem. **19**, 710–717 (2012).
[94]G. Mancuso, M. Langone, and G. Andreottola, "A swirling jet-induced cavitation to increase activated sludge solubilisation and aerobic sludge biodegradability," Ultrason. Sonochem. **35**, 489–501 (2017).
[95]P. Suryawanshi, V. Bhandari, L. Sorokhaibam, J. Ruparelia, and V. V. Ranade, "Solvent degradation studies using hydrodynamic cavitation," Env. Prog. Sustain. Energy **37**, 295–304 (2018).
[96]S. Jahangir, W. Hogendoorn, and C. Poelma, "Dynamics of partial cavitation in an axisymmetric converging–diverging nozzle," Int. J. Multiphase Flow **106**, 34–45 (2018).
[97]M. Poorbaba and M. Soleimani, "Full three-dimensional computational fluid dynamics simulation and optimization of a swirling jet-induced cavitation reactor," Phys. Fluids **35**, 083307 (2023).
[98]A. Mancuso, A. Aquila, L. Batchelor, R. Bean, J. Bielecki, G. Borchers, K. Doerner, K. Giewekemeyer, R. Graceffa, O. Kelsey, Y. Kim, H. J. Kirkwood, A. Legrand, R. Letrun, B. Manning, L. L. Morillo, M. Messerschmidt, G. Mills, S. Raabe, N. Reimers, A. Round, T. Sato, J. Schulz, C. Takem, M. Sikorski, S. Stern, P. Thute, P. Vagovič, B. Weinhausen, and T. Tschentscher, "The single particles, clusters and biomolecules and serial femtosecond crystallography instrument of the European XFEL: Initial installation," J. Synchrotron Rad. **26**, 660–676 (2019).
[99]P. Vagovič, T. Sato, L. Mikeš, G. Mills, R. Graceffa, F. Mattsson, P. Villanueva-Perez, A. Ershov, T. Faragó, J. Uličný, H. J. Kirkwood, R. Letrun, R. Mokso, M. Zdora, M. Olbinado, A. Rack, T. Baumbach, J. Schulz, A. Meents, and A. Mancuso, "Megahertz x-ray microscopy at x-ray free-electron laser and synchrotron sources," Optica **6**, 1106–1109 (2019).
[100]J. C. P. Koliyadu, D. Moško, E. M. Asimakopoulou, V. Bellucci, Š. Birnšteinová, R. Bean, R. Letrun, C. Kim, H. Kirkwood, G. Giovanetti, N. Jardon, J. Szuba, T. Guest, A. Koch, J. Grünert, P. Szeles, P. Villanueva-Perez, F. Reuter, C.-D. Ohl, M. A. Noack, F. Garcia-Moreno, Z. Kuglerová-Valdová, L. Juha, M. Nikl, W. Yashiro, H. Soyama, D. Eakins, A. M. Korsunsky, J. Uličný, A. Meents, H. N. Chapman, A. P. Mancuso, T. Sato, and P. Vagovič, "Development of MHz x-ray phase contrast imaging at the European XFEL," J. Synchrotron Rad. **32**, 17 (2025).
[101]C. Stanley, T. Barber, B. Milton *et al.*, "Periodic cavitation shedding in a cylindrical orifice," Exp. Fluids **51**, 1189–1200 (2011).
[102]J. N. Ridler and S. Calvard, "Picture thresholding using an iterative selection method," IEEE Trans. Syst. Man Cybern. **8**, 630–632 (1978).
[103]N. Otsu, "A threshold selection method from gray-level histograms," IEEE Trans. Syst. Man Cybern. **9**, 62–66 (1979).
[104]S. Grundmann, F. Wassermann, R. Lorenz, B. Jung, and C. Tropea, "Experimental investigation of helical structures in swirling flows," Int. J. Heat Fluid Flow **37**, 51–63 (2012).
[105]M. Shahsavari, M. Farshchi, and M. Arabnejad, "Large eddy simulations of unconfined non-reacting and reacting turbulent low swirl jets," Flow. Turbul. Combust. **98**, 817–840 (2017).
[106]Y. Zhang and M. Vanierschot, "Determination of single and double helical structures in a swirling jet by spectral proper orthogonal decomposition," Phys. Fluids **33**, 015115 (2021).
[107]Y. D. Chizelle, S. E. Ceccio, and C. E. Brennen, "Observations and scaling of travelling bubble cavitation," J. Fluid Mech. **293**, 99–126 (1995).
[108]C. Li and S. E. Ceccio, "Interaction of single travelling bubbles with the boundary layer and attached cavitation," J. Fluid Mech. **322**, 329–353 (1996).
[109]K. R. Laberteaux, S. E. Ceccio, V. Mastrocola, and J. Lowerance, "High speed digital imaging of cavitating vortices," Exp. Fluids **24**, 489–498 (1998).
[110]X. Tian, Z. Li, and Z. Qian, "Effect of dissolved air content on attached cavitation in a venturi section," Phys. Fluids **37**, 013355 (2025).
[111]J. Venning, B. W. Pearce, and P. A. Brandner, "Nucleation effects on cloud cavitation about a hydrofoil," J. Fluid Mech. **947**, A1 (2022).
[112]J. Luo, W. Xu, and B. C. Khoo, "Stratification effect of air bubble on the shock wave from the collapse of cavitation bubble," J. Fluid Mech. **919**, R2 (2021).

22 April 2026 09:41:02

© Author(s) 2026